

In situ Measurement of Curvature of Magnetic Field in Turbulent Space Plasmas: A Statistical Study

RIDDHI BANDYOPADHYAY,^{1,2} YAN YANG,^{3,4} WILLIAM H. MATTHAEUS,^{1,2} ALEXANDROS CHASAPIS,⁵ TULASI N. PARASHAR,^{1,2}
CHRISTOPHER T. RUSSELL,⁶ ROBERT J. STRANGWAY,⁶ ROY B. TORBERT,⁷ BARBARA L. GILES,⁸ DANIEL J. GERSHMAN,⁸
CRAIG J. POLLOCK,⁹ THOMAS E. MOORE,⁸ AND JAMES L. BURCH¹⁰

¹*Department of Physics and Astronomy, University of Delaware, Newark, DE 19716, USA*

²*Bartol Research Institute, University of Delaware, Newark, DE 19716, USA*

³*Southern University of Science and Technology, Shenzhen, Guangdong 518055, China*

⁴*University of Science and Technology of China, Hefei, Anhui 230026, China*

⁵*Laboratory for Atmospheric and Space Physics, University of Colorado Boulder, Boulder, Colorado, USA*

⁶*University of California, Los Angeles, California 90095-1567, USA*

⁷*University of New Hampshire, Durham, New Hampshire 03824, USA*

⁸*NASA Goddard Space Flight Center, Greenbelt, Maryland 20771, USA*

⁹*Denali Scientific, Fairbanks, Alaska 99709, USA*

¹⁰*Southwest Research Institute, San Antonio, Texas 78238-5166, USA*

(Received March 31, 2020)

ABSTRACT

Using in situ data, accumulated in the turbulent magnetosheath by the *Magnetospheric Multiscale* (*MMS*) Mission, we report a statistical study of magnetic field curvature and discuss its role in the turbulent space plasmas. Consistent with previous simulation results, the Probability Distribution Function (PDF) of the curvature is shown to have distinct power-law tails for both high and low value limits. We find that the magnetic-field-line curvature is intermittently distributed in space. High curvature values reside near weak magnetic-field regions, while low curvature values are correlated with small magnitude of the force acting normal to the field lines. A simple statistical treatment provides an explanation for the observed curvature distribution. This novel statistical characterization of magnetic curvature in space plasma provides a starting point for assessing, in a turbulence context, the applicability and impact of particle energization processes, such as curvature drift, that rely on this fundamental quantity.

Keywords: plasmas — turbulence

1. INTRODUCTION

The curvature of the magnetic field enters in numerous important ways in electrodynamics (Petschek 1964) and plasma physics (Boozer 2005), representing one of the principle ways that magnetic fields interact with matter. Curvature plays a key role in magnetic reconnection (Petschek 1964), stability of magnetic confinement (Dobrott et al. 1977), in magnetospheric physics and space physics (Hameiri et al. 1991), and in particle heating and acceleration (Jokipii 1982; Pesses et al. 1981; Dahlin et al. 2014). Usually, curvature is studied with regard to specific magnetic configurations. For

example, stability with respect to ballooning modes requires favorable curvature that is antiparallel to the pressure gradients (Boozer 2005). Similarly, the large curvature of field lines in reconnection exhausts gives rise to relaxation towards a less stressed state, leading to electron energization by curvature drift acceleration (Dahlin et al. 2014). Magnetic-field curvature has been useful for detecting helical field configuration of flux ropes from in situ measurements (Slavin et al. 2003; Shen et al. 2007; Sun et al. 2019).

Recently, the curvature of magnetic field lines has been studied in the magnetohydrodynamic (MHD) model of plasma turbulence (Yang et al. 2019). In the case of turbulence, it is impractical to study curvature of individual field lines and one may resort to a statistical approach, as is typical in studies of turbulence (Monin &

Yaglom 1971). In these simulations, one finds interesting properties such as a distribution of curvature that exhibits two power-law regimes, and a systematic anticorrelation of curvature with magnetic field strength, for low values of magnetic field strength. Here, we extend this statistical examination of magnetic curvature by analysis of *in situ* satellite observations in the terrestrial magnetosheath. We employ *Magnetospheric Multiscale (MMS)* data that reveal distributions and correlations that are consistent with, and in fact very similar to, those observed in the MHD simulations (Yang et al. 2019). These results confirm the theoretical model given in Yang et al. (2019), opening the door to new applications such as curvature drift acceleration in turbulence as well as the possible role of local explosive instabilities in turbulence.

The outline of the paper is as follows: in Sec. 2, we discuss the theoretical derivation and approximations. In Sec. 3, we apply the theoretical constructs to MMS data and present the results. We discuss the importance of the results and conclude in Sec. 4. In Appendix A, B, we justify the assumptions made in Sec. 2. Appendix C shows the results presented in Sec 3 for a different MMS interval.

2. THEORY AND METHOD

The curvature κ of magnetic field \mathbf{B} is defined as

$$\kappa = |\mathbf{b} \cdot \nabla \mathbf{b}|, \quad (1)$$

where $\mathbf{b} = \mathbf{B}/B$ and $B = |\mathbf{B}|$. It can be expressed also in the form

$$\begin{aligned} \kappa &= \frac{|\mathbf{b} \times (\mathbf{B} \cdot \nabla \mathbf{B})|}{B^2} \\ &= \frac{f_n}{B^2}, \end{aligned} \quad (2)$$

where $f_n = |\mathbf{b} \times (\mathbf{B} \cdot \nabla \mathbf{B})|$ is the magnitude of the tension force (per unit volume) acting normal to the field lines. In the curvilinear coordinate attached to a field line, traced by a trajectory $\gamma(s)$, the scalar s is a coordinate along the field line, while $\mathbf{e}_t = \frac{d\gamma}{ds}/|\frac{d\gamma}{ds}| = \mathbf{b}$ and $\mathbf{e}_n = \frac{d^2\gamma}{ds^2}/|\frac{d^2\gamma}{ds^2}|$ are the unit vectors in the tangential and normal directions along the field line, respectively. Then

$$\mathbf{B} \cdot \nabla \mathbf{B} = (B\mathbf{e}_t) \cdot \nabla (B\mathbf{e}_t) = B \frac{\partial(B\mathbf{e}_t)}{\partial s} = B \frac{\partial B}{\partial s} \mathbf{e}_t - \kappa B^2 \mathbf{e}_n \quad (3)$$

Equation (2) follows directly from Eq. (3).

It is shown in the following section that high curvature values are well associated with weak magnetic field. In contrast, low curvature values mainly result from small

normal force, more so than from large values of magnetic field. These findings point the way to explain the power-law tails in the curvature distribution in both the high value range, and the low value range, reasoning as follows Yang et al. (2019).

First, let us consider the low value range. Noting that the normal force is two-dimensional, we write its cartesian components as f_1 and f_2 , and then assume that these are independent random variables and their PDFs for small values obey Gaussian distribution. Then the PDFs of f_1 and f_2 at small values may be written as

$$P_{f_1}(f) = P_{f_2}(f) = \frac{1}{\sqrt{2\pi\sigma_1^2}} e^{-\frac{f^2}{2\sigma_1^2}}, \quad (4)$$

where, f denotes the value of either f_1 or f_2 at the point of interest, and σ_1^2 is the variance. The quantity $f_n^2/\sigma_1^2 = (f_1^2 + f_2^2)/\sigma_1^2$ should then be distributed according to the chi-squared distribution with 2 degrees of freedom. The corresponding PDF of f_n at small values (i.e. $f_n \rightarrow 0$) is

$$P_{f_n}(f) = \frac{f}{\sigma_1^2} e^{-\frac{f^2}{2\sigma_1^2}}. \quad (5)$$

Here, f represents the value of the variable f_n . See Appendix A where a slightly more general, but equivalent, development is given. Since $\kappa = f_n B^{-2}$ and low curvature κ is determined by the scaling behavior of small normal force f_n , the PDF of curvature as $\kappa \rightarrow 0$ can be written as

$$P_\kappa(\kappa') = B^2 P_{f_n}(\kappa' B^2) = \frac{B^4 \kappa'}{\sigma_1^2} e^{-\frac{B^4 \kappa'^2}{2\sigma_1^2}}. \quad (6)$$

Here, κ' is the value of the variable κ . Let us assume that B is finite in this limit, which could be replaced with B_{rms} in equation (6). Then the Taylor series of the PDF around $\kappa' = 0$ is

$$\frac{B^4}{\sigma_1^2} \left(\kappa' - \frac{B^4}{2\sigma_1^2} \kappa'^3 + \dots \right). \quad (7)$$

The higher-degree terms are much smaller as $\kappa' \rightarrow 0$, so we retain only the lowest order term, and obtain

$$P_{\kappa \rightarrow 0}(\kappa') \sim \kappa'^1. \quad (8)$$

In a similar way, we can explain the power-law tail of the PDF for high curvature values. In isotropic turbulence, we suppose that x , y , and z components of magnetic fluctuations are independent Gaussian random variables. Then

$$B_x, B_y, B_z \sim \mathcal{N}(0, \sigma_2^2), \quad (9)$$

where $\mathcal{N}(0, \sigma_2^2)$ denotes the normal distribution with mean 0 and variance σ_2^2 . In real systems, the magnetic fields are never fully isotropic, so we eliminate the average from each component and work with the fluctuations. Note that, in a turbulent system, the *increments* of the magnetic field are intermittently distributed with super-Gaussian tails (Matthaeus et al. 2015), but the fluctuation components themselves are rather well described by Gaussian distribution (Batchelor 1951; Padhye et al. 2001, also see Appendix B). The quantity $B^2/\sigma_2^2 = (B_x^2 + B_y^2 + B_z^2)/\sigma_2^2$, therefore, follows the chi-squared distribution with 3 degrees of freedom. The corresponding PDF of B^2 is

$$P_{B^2}(b') = \frac{\sqrt{b'}}{(2\sigma_2^2)^{3/2} \Gamma(3/2)} e^{-\frac{b'}{2\sigma_2^2}}, \quad (10)$$

where, b' represents the value of B^2 at the point of interest, and Γ is the gamma function. Since $\kappa = f_n B^{-2}$ and high curvature κ is determined by the scaling behavior of weak magnetic field B^2 , the PDF of curvature as $\kappa \rightarrow \infty$ can be written as

$$P_\kappa(\kappa') = \frac{f_n}{\kappa'^2} P_{B^2}\left(\frac{f_n}{\kappa'}\right) = \frac{f_n^{3/2} \kappa'^{-5/2}}{(2\sigma_2^2)^{3/2} \Gamma(3/2)} e^{-\frac{f_n}{2\sigma_2^2 \kappa'}} \quad (11)$$

Again, κ' is the value of the variable κ . In analogy to the prior case, we assume that f_n remains finite in this limit, and replace the associated value with the average $\langle f_n \rangle$ in equation (11). Then the Taylor series for the PDF about $1/\kappa' = 0$ becomes,

$$\frac{f_n^{3/2}}{(2\sigma_2^2)^{3/2} \Gamma(3/2)} \left(\kappa'^{-5/2} - \frac{f_n}{2\sigma_2^2} \kappa'^{-7/2} + \dots \right). \quad (12)$$

It follows that in the limit as $\kappa' \rightarrow \infty$, i.e. $1/\kappa' \rightarrow 0$, the curvature PDF scales as

$$P_{\kappa \rightarrow \infty}(\kappa') \sim \kappa'^{-5/2}. \quad (13)$$

Previously (Yang et al. 2019), the above reasoning was found to explain the behavior of the distributions of curvature in three dimensional, isotropic, MHD simulations. We now extend this inquiry to the case of a naturally occurring space plasma, the turbulent magnetosheath.

Below, we use four-spacecraft linear estimates of gradient, similar to the ‘‘curlometer’’ method (Dunlop et al. 1988; Paschmann & Daly 1998) to calculate $\nabla \mathbf{b}$. Then a dot product with \mathbf{b} yields the curvature $\kappa = |\mathbf{b} \cdot \nabla \mathbf{b}|$. In section 3, we use this approach to analyze the statistical properties of the curvature field using *MMS* observations, including the accuracy of the above scaling arguments.

Table 1. Description of *MMS* Dataset from 06:12:43 to 06:52:23 UTC on 26 December 2017. The quantities are defined in the text.

MMS position (X, Y) _{GSE}	$ \langle \mathbf{B} \rangle $ (nT)	$B_{\text{rms}}/ \langle \mathbf{B} \rangle $	L (km)	d_i (km)	β_p
(10 R _e , 9 R _e)	17.9	0.8	27	47	4.4

3. *MMS* OBSERVATIONS

MMS consists of four identical spacecraft orbiting the Earth, for the chosen period, in a tetrahedral formation with small (~ 10 km) separation. The four *MMS* spacecraft sample the near-Earth plasma including the magnetosheath (Burch et al. 2016). The Fast Plasma Investigation (FPI) (Pollock et al. 2016) instrument calculates the proton and electron three dimensional velocity distribution functions (VDF) and the Flux-Gate Magnetometer (FGM) (Russell et al. 2016) measures the vector magnetic field.

In burst mode, the Dual Ion Spectrometer (DIS) and the Dual Electron Spectrometer (DES) in FPI/*MMS* measure the ion and electron VDF at cadence of 150 ms and 30 ms, respectively. Plasma moments are calculated from each VDF at the corresponding time resolution. The time resolution of the FGM magnetic field is 128 Hz in burst mode.

To cover a large statistical sample of the turbulent plasma in the magnetosheath, here we focus on one long *MMS* burst-mode interval between 06:12:43 and 06:52:23 UTC on 26 December 2017. A time series plot of the selected interval is shown in figure 1. The FGM magnetic field components, in geocentric solar ecliptic (GSE) coordinate system (Franz & Harper 2002), are shown in panel (a). The magnetic field components exhibit large-amplitude fluctuations which is typical for magnetosheath plasma. The electron density estimates are often more accurate than the ion density in the magnetosheath due to higher thermal speed. Panel (b) plots the electron density, obtained from the FPI/DES distributions. The three GSE components of the ion velocity components, measured by FPI/DIS, are plotted in panel (c). The final panel (d), shows the time series of the curvature field, derived from the magnetic field by a finite difference curlometer-like method (see Section 2). The curvature values are observed to be highly intermittent with thin ‘‘spikes’’ distributed during the whole interval that suggest the presence of sheet-like structures.

Several important plasma parameters of the selected *MMS* interval are reported in Table 1, including the locations of the *MMS* spacecraft in GSE coordinate system, in units of Earth radius (R_E) during the in-

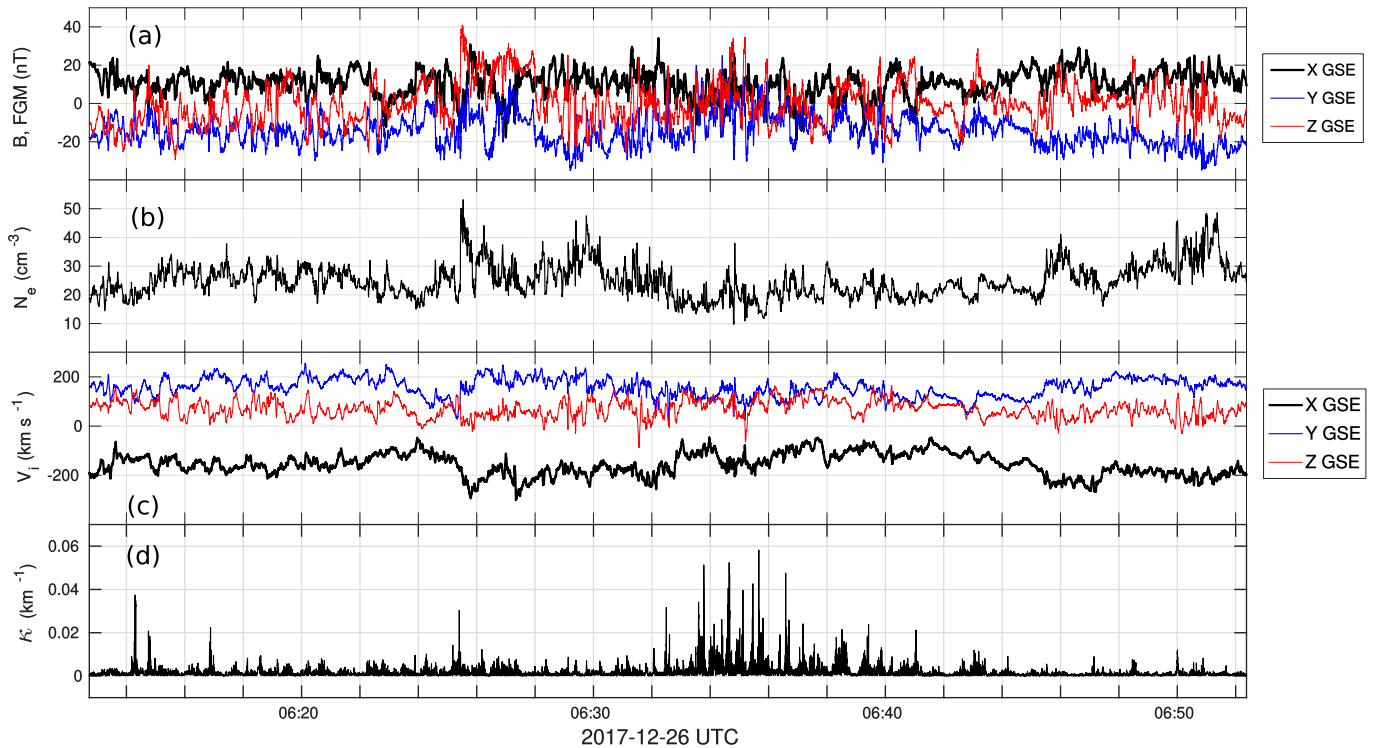


Figure 1. Overview of the *MMS* observations in turbulent magnetosheath selected for this study. The data shown are from the FGM and FPI instruments on-board the *MMS1* spacecraft. Panel (a) shows the magnetic field measurements in GSE coordinates. Panel (b) shows the electron density. Panel (c) shows the ion velocity in GSE coordinates. Panel (d) shows the curvature calculated (approximately using a curlometer-like method) from the magnetic field (see equation (1)).

interval, mean magnetic field ($|\langle \mathbf{B} \rangle|$), ratio of rms fluctuation amplitude of the magnetic field (B_{rms}) to the mean magnetic field, average spacecraft separation L , ion-inertial length (d_i), and the average plasma beta (β_p). The rms fluctuation amplitude is defined as $B_{\text{rms}} = \sqrt{\langle |\mathbf{B}(t) - \langle \mathbf{B} \rangle|^2 \rangle}$, which has a value of 14 nT here. The density fluctuation amplitude is similarly defined. Note that the density fluctuations are rather low, comparable to the typical values observed in the interplanetary solar wind. The spacecraft separations are much smaller than the ion-inertial length. However, using the curlometer method in the determination of gradients, there are some errors associated, which affect the estimation of f_n and κ . Following (Shen et al. 2003) and Shen et al. (2007), the fractional error in the curvature values can be estimated roughly as,

$$\frac{\Delta \kappa}{\kappa} \sim \mathcal{O}(L\kappa), \quad (14)$$

where L is the spacecraft separation. For the present interval, if we use $L \sim 10$ km, and from Fig. 1, the maximum of curvature values reaches about $\kappa \sim 0.5 \text{ km}^{-1}$. Therefore, the fractional error in curvature remains within ~ 0.5 . Further, by comparing the FPI current and curlometer current, several studies have found

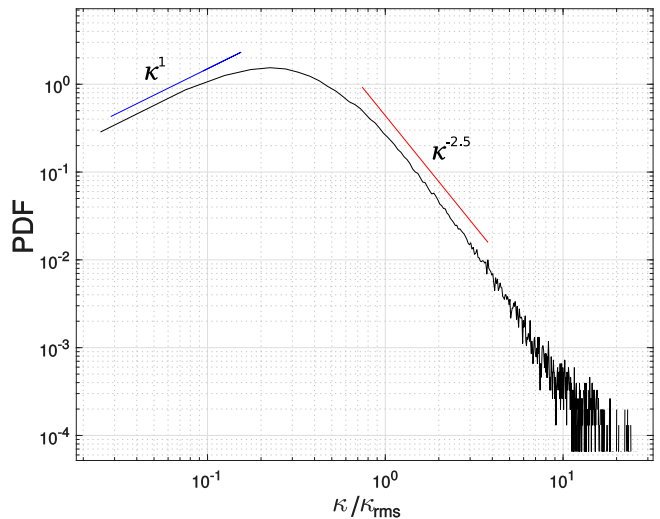


Figure 2. PDF of the magnetic field curvature κ normalized to its rms value κ_{rms} , computed from the 40 minute *MMS* dataset shown in Fig. 1.

that *MMS* curlometer usually works well in the magnetosheath (e.g., Gershman et al. 2018; Stawarz et al. 2019). Therefore, the results presented below are expected to be reliable.

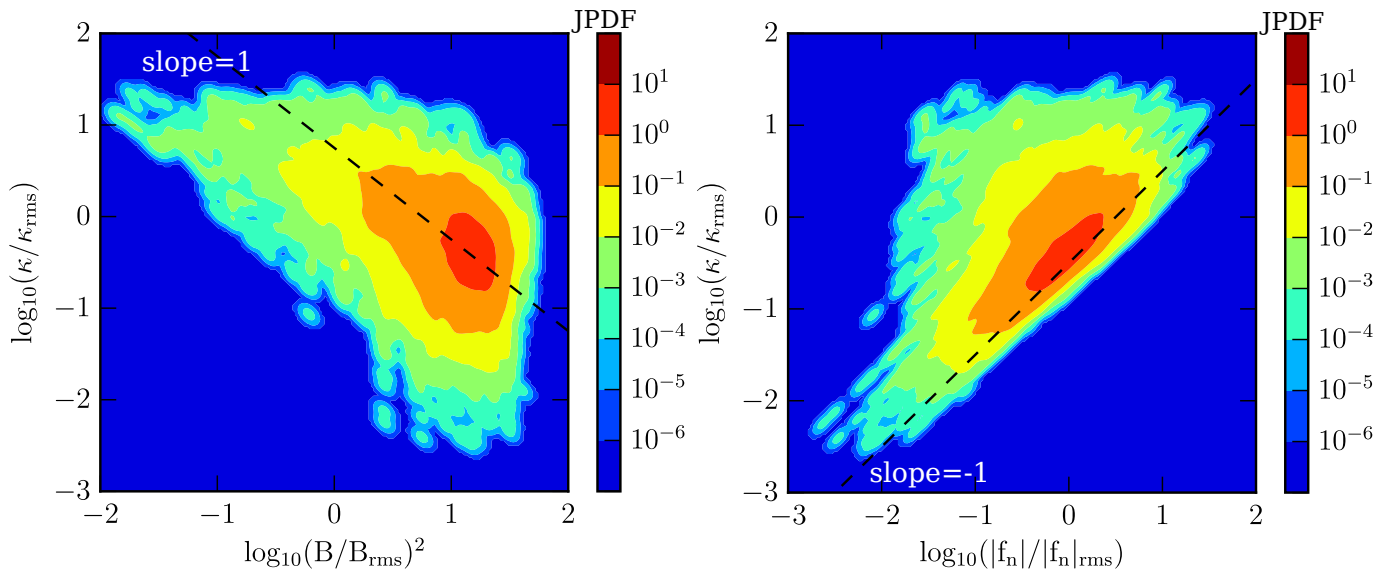


Figure 3. Joint PDFs of curvature κ and (left panel): the square of magnetic field magnitude B^2 , and (right panel): the magnitude of the force $|f_n|$ acting normal to the field lines. All quantities are normalized to their respective rms values. Dashed lines with slope of 1 and -1 are shown for reference.

The main quantitative observational result of this study is contained in Fig. 2, which shows the probability distribution function of the curvature for the ≈ 40 minute magnetosheath interval of MMS data described in Table 1 and shown in Fig. 1. Many prior studies (e.g., Slavin et al. 2003; Shen et al. 2003, 2007; Rong et al. 2011; Sun et al. 2019; Akhavan-Tafti et al. 2019) have explored curvature of the magnetic field in the magnetosphere for individual events or collection of structures, but as far as we are aware, this is the first detailed analysis of *statistics* of magnetic-field curvature in turbulent space plasmas using observational data.

The probability distribution function shown in figure 2, exhibits two distinct powerlaw regimes: at low values of the curvature field, its distribution scales roughly as κ^{+1} , while at high curvature values the distribution behaves as $\kappa^{-2.5}$. This is remarkably similar to the empirical and theoretical findings of Yang et al. (2019).

To further clarify the statistics of the magnetic curvature, Fig. 3 shows the joint probability distributions of curvature and squared magnetic field magnitude, and curvature and normal force. The relationship between high curvature and regions of weak magnetic field is corroborated by the former. In Fig. 2, the power-law regimes are separated at $\kappa/\kappa_{\text{rms}} \lesssim 0.1$ and $\kappa/\kappa_{\text{rms}} \gtrsim 1$. From the left panel of Fig. 3, the curvature and magnetic field are rather well associated for $\kappa/\kappa_{\text{rms}} \gtrsim 1$ and the association begins to weaken at $\kappa/\kappa_{\text{rms}} \lesssim 0.1$. The Pearson-r coefficient between $\kappa/\kappa_{\text{rms}}$ and $(B/B_{\text{rms}})^2$ for $\kappa/\kappa_{\text{rms}} \geq 0.9$ has a magnitude of 0.53 and it is 0.005 for $\kappa/\kappa_{\text{rms}} \leq 0.15$. This is consistent with the intuition

Table 2. Pearson’s-r coefficient between curvature and magnetic field strength, and normal force for low and high curvature ranges.

		Range	
		$\kappa/\kappa_{\text{rms}} \leq 0.15$	$\kappa/\kappa_{\text{rms}} \geq 0.9$
Variables	$\kappa/\kappa_{\text{rms}}, (B/B_{\text{rms}})^2$	$r = 0.005$	$r = -0.53$
	$\kappa/\kappa_{\text{rms}}, f_n / f_n _{\text{rms}}$	$r = 0.12$	$r = 0.02$

that weak magnetic fields are easier to bend, and leads to the above-described $\kappa^{-2.5}$ curvature distribution in the weak magnetic field regime.

Similarly, the positive correlation between curvature and normal force per unit volume at low curvature is in Fig. 3, right panel. Again, at small curvature values, κ and f_n are well correlated with a Pearson-r coefficient value of 0.12 for $\kappa/\kappa_{\text{rms}} \leq 0.15$. However, at high-curvature value the association is not so clear, resulting in a Pearson-r value of 0.02 for $\kappa/\kappa_{\text{rms}} \geq 0.9$. This supports the reasoning that leads to the κ^{+1} behavior of the κ distribution at the small values of curvature. These quantifications are summarized in Table 2.

The interval shown in Fig. 1 is selected for no special reason other than its long duration and the preliminary observation that it exhibits well-developed turbulence properties (Parashar et al. 2018). Same analyses on other turbulent magnetosheath intervals produce similar results (see Appendix C and Fig. 7).

As a final, direct observational diagnostic, in the two panels in Fig. 4 we show small samples of the time series of curvature and magnetic field (top panel), and curva-

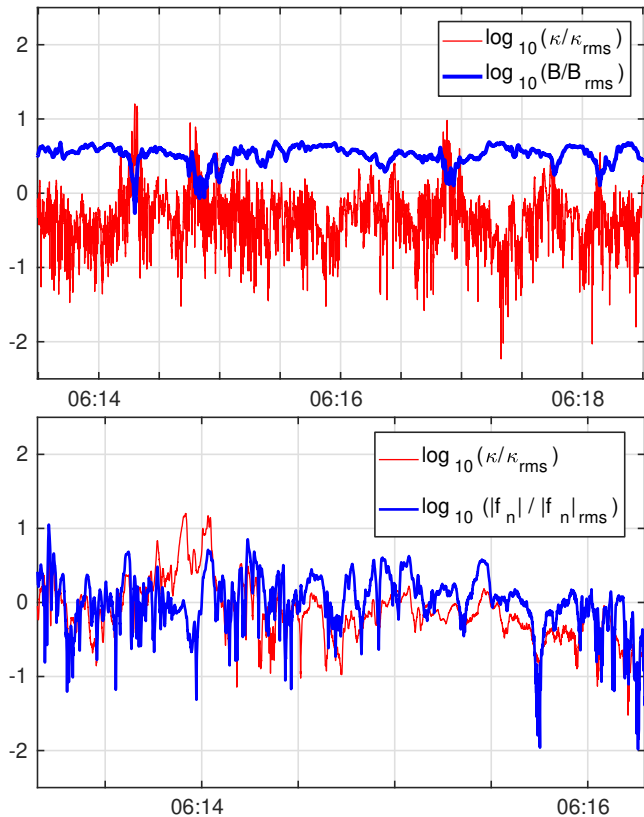


Figure 4. Time series of the curvature field, in thin red line, superposed on the magnetic-field magnitude (Top panel) and the magnitude of the normal force (Bottom panel), in broad blue line, and for a small subinterval of the whole magnetosheath interval.

ture and the normal force (bottom panel). to illustrates how large (small) curvature regions are often localized in regions of low magnetic field strength (low normal force strength).

Indeed, from the top panel in Fig. 4 one observes several *peaks* in curvature values that are contemporaneous with sharp drops in the magnetic field strength. Similarly, from the bottom panel, strong *dips* in the curvature is accompanied by dips in the normal force values. For clarity, only small subintervals of the whole magnetosheath intervals are shown. We note that only curvature large enough, say $\kappa/\kappa_{\text{rms}} \gtrsim 1$ (i.e., the right power-law regime in Fig. 2), is associated with small B , and only curvature small enough, say $\kappa/\kappa_{\text{rms}} \lesssim 0.1$ (i.e., the left power-law regime in Fig. 2), is associated with small f_n . This behavior is also consistent with the trends seen in Fig. 3 and Table 2.

4. DISCUSSION

Employing the unique capabilities of the *MMS* mission, we have studied the statistical properties of the

curvature of the magnetic field measured in the terrestrial magnetosheath by the FGM instrument onboard each of the four spacecraft. The dataset employed is a long, 40 minute duration, burst mode interval in the terrestrial magnetosheath. This determination of the statistical character of the magnetic curvature is the first of its kind in a space plasma, as far as we are aware.

We find two powerlaw regimes in the distribution of values of curvature: a κ^{+1} regime at low κ , and a $\kappa^{-2.5}$ regime at large κ . We also find an anticorrelation of curvature and magnetic field strength at low magnetic field strength, and a positive correlation of curvature and normal force per unit volume at small values of the force. All of these results are consistent with the findings of Yang et al. (2019), based on MHD simulations. What is more remarkable is the degree of quantitative agreement of the present observations with the MHD results. The simple theory outlined here, clearly is adequate to explain the two powerlaw ranges in the curvature that are seen in both simulations and observations.

It is interesting to note that the kind of distribution we find for curvature (Fig. 2) has been studied in applied mathematics and is known as a “double Pareto” distributions (Reed 2001; Reed & Hughes 2002; Reed & Jorgensen 2004; Fang et al. 2012), generalizing the standard nomenclature of Pareto distribution for a range of scale invariant power law behavior (Mitzenmacher 2004). This type of distribution generally indicates a multiplicative process. However, if such a process is uninhibited it leads to a log normal distributions. When a physical effect, such as the inner scale of turbulence, or the particle gyro motion changes the physics and limits the process, it becomes a double-Pareto. The mathematics of such processes may provide fruitful directions for additional study of the nature of magnetic field curvature and its effects on particle acceleration.

One possibility that presents itself is that these results may be applicable to turbulent magnetic fields in other venues including other heliospheric environments and perhaps in astrophysical contexts as well. We note that, in order to derive the power-law scalings, equations (8) and (13), we assume that the magnetic field components are isotropically distributed. Real systems are never perfectly isotropic at any length scale, but the magnetosheath conditions are rather close to isotropy with a weak DC field (see figure 1 and table 1). Extending the present study to other plasma systems, e.g., solar wind, magnetotail, magnetosphere, etc., would require appropriate modification to the derivation, although the basic arguments are expected to remain unchanged. Independent confirmation from other simulations, laboratory experiments, as well as other observations, if avail-

able, is called for. To the extent that these results are robust, at least one major theoretical application is suggested. Specifically, curvature drift acceleration theory (e.g., Hoshino et al. 2001; Dahlin et al. 2014; Guo et al. 2015), has apparently been very successful in explaining electron energization in individual magnetic reconnection events. Since this theory depends explicitly on κ , one would expect that an immediate extension based on the present results would be to include a statistical distribution of curvature values, to develop a curvature drift energization mechanism appropriate to magnetized plasma turbulence.

ACKNOWLEDGMENTS

This research was partially supported by NASA under the Magnetospheric Multiscale Mission (*MMS*) Theory and Modeling program grant NNX14AC39G and by NASA Heliospheric Supporting Research Grant NNX17AB79G. We would like to acknowledge the assistance of the *MMS* instrument teams, especially FPI and FIELDS, in preparing the data, as well as the work done by the *MMS* Science Data Center (SDC). The data used in this work are Level 2 FIELDS data products, in cooperation with the instrument teams and in accordance with their guidelines. All *MMS* data used in this study are publicly available at the *MMS* Science Data Center (<https://lasp.colorado.edu/MMS/sdc/public/>). The Interplanetary Magnetic Field (IMF) data, measured by the *Wind* spacecraft, are used to determine the angle between the shock normal and the IMF in Appendix B. The IMF, shifted to Earth's bow-shock nose, can be found at <https://omniweb.gsfc.nasa.gov/>. The authors thank the *Wind* team for the *Wind* magnetic field data.

APPENDIX

A. DISTRIBUTION OF NORMAL FORCE AT SMALL VALUES

In deriving the scaling properties of curvature, κ , at low- κ values (Eq. 8), we assume that the normal force components f_1 and f_2 are independent Gaussian variables for small values. However, the only result that is actually used in the subsequent development is Eq. 5 which is the distribution of the values of the *magnitude* of the normal force, f_n . The exact form of the distributions of f_1 and f_2 , therefore, is not a salient point. Rather, if f_n follows a chi-squared distribution with 2 degrees of freedom (Eq. 5) for small values of f_n , that would support the subsequent development of the theory. Fig. 5 shows the distribution of f_n and compares it with Eq. 5 for the interval analyzed in the main text. It is evident that the small values of normal force are well described by Eq. 5.

B. DISTRIBUTION OF MAGNETIC-FIELD COMPONENTS IN THE MAGNETOSHEATH PLASMA

In deriving the scaling properties of curvature, κ , at high- κ values (Eq. 13), we assume that the probability distribution of magnetic-field components is approximately Gaussian, e.g., in Eq. 9. Although established in the pristine solar wind at 1 au (Padhye et al. 2001), and expected in general for primitive variables in turbulence (Batchelor

1951), the Gaussianity of the turbulent fluctuations in the magnetosheath has not been previously quantified, as far as we are aware (although see Whang 1977). To justify this approximation, here we examine the probability distribution functions (PDFs) of the fluctuations of the magnetic field components using analysis of several *MMS* data sets. Functional fits as well as moment comparisons (kurtoses) are used in drawing conclusions concerning the degree of non-Gaussianity.

To begin, we analyze the main 40 minute data interval analyzed in the text, shown in Fig. 1 and described in Table 1. The data from each spacecraft are rank-ordered into 100 bins of variable width such that each bin has an equal number of data points. For each component, data from all 4 spacecraft are collected together to increase the statistical weight. The density of points in each bin provides an approximation to the PDFs, This procedure is carried out for the fluctuating magnetic-field components, and these empirically determined PDFs are shown in Fig. 6. The solid curves are the corresponding Gaussian PDFs with zero mean and a variance equal to that computed from the data. The goodness of fit is measured by χ^2 , defined as

$$\chi^2 = \frac{\sum_i [f(a_i) - g(a_i)]^2 \Delta a_i}{\sum_i [f(a_i)]^2 \Delta a_i}, \quad (\text{B1})$$

where $f(a_i)$ is the observed PDF of any magnetic-field component, and $g(a_i)$ is the corresponding Gaussian distribution. For a perfect agreement ($f = g$), $\chi^2 = 0$; small value of χ^2 indicates satisfactory fitness.

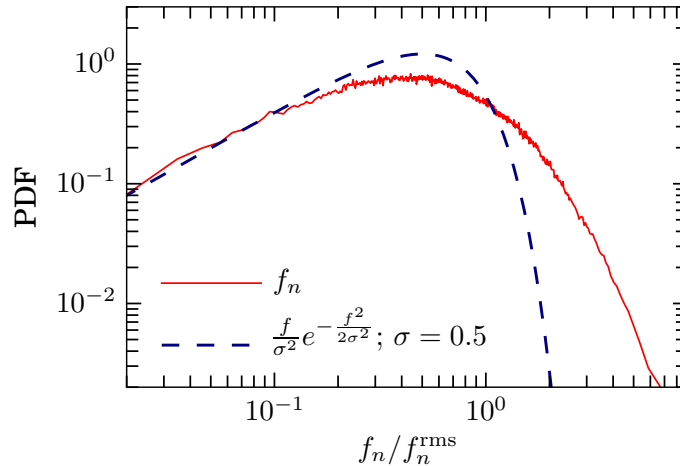


Figure 5. PDFs of the value of the normal force f_n as computed from *MMS* data analyzed using a 40-minute interval.

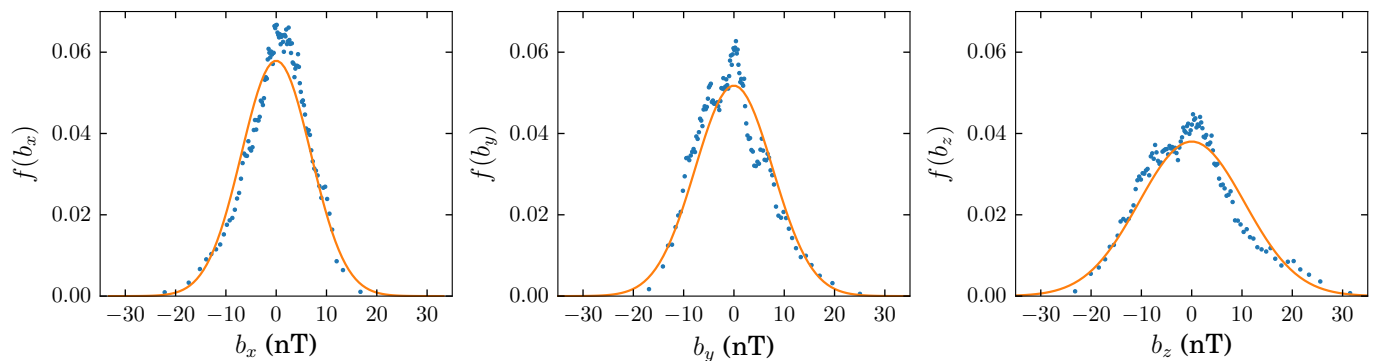


Figure 6. PDFs of fluctuations of the magnetic field as computed from *MMS* data analyzed using a 40-minute interval. X, Y, and Z components are shown in top, middle, and bottom panel. The dots represent centers of the binned data, and the solid line shows the reference Gaussian. Each of the 100 bins contains 15373 measurements.

Table 3. Kurtoses and χ^2 values for the magnetic field components measured by *MMS* in the magnetosheath.

Interval	MMS position (X, Y) _{GSE}	Parameter	b_x	b_y	b_z	$B_{\text{rms}}/ \langle \mathbf{B} \rangle $	Shock Type
26 December 2017, 06:12:43 - 06:52:23	(10 R _e , 9 R _e)	χ^2	0.018	0.023	0.023	0.8	quasi-
		Kurtosis	3.56	3.50	3.23		
11 January 2016, 00:57:04 - 01:00:34	(9 R _e , -8 R _e)	χ^2	0.031	0.020	0.067	1.5	quasi-⊥
		Kurtosis	3.76	3.06	4.5		
18 January 2017, 00:45:54 - 00:49:42	(8 R _e , -5 R _e)	χ^2	0.020	0.067	0.113	1.8	quasi-
		Kurtosis	2.77	2.43	3.56		
27 January 2017, 08:02:03 - 08:08:03	(11 R _e , 6 R _e)	χ^2	0.04	0.09	0.02	2.1	quasi-
		Kurtosis	3.14	3.08	3.29		
21 December 2017, 06:41:55 - 07:03:51	(13 R _e , -1 R _e)	χ^2	0.085	0.022	0.019	2.1	quasi-
		Kurtosis	3.23	2.92	2.75		
21 December 2017, 07:21:54 - 07:48:01	(14 R _e , 0 R _e)	χ^2	0.012	0.094	0.045	1.9	quasi-
		Kurtosis	4.03	2.83	2.61		
19 April 2018, 05:08:04 - 05:41:51	(-3 R _e , -22 R _e)	χ^2	0.011	0.014	0.011	3.1	quasi-⊥
		Kurtosis	3.41	3.81	3.46		
23 April 2018, 07:50:14 - 08:33:41	(3 R _e , 18 R _e)	χ^2	0.019	0.035	0.027	1	quasi-⊥
		Kurtosis	3.54	3.47	3.73		
27 October 2018, 09:13:14 - 09:57:41	(-2 R _e , 24 R _e)	χ^2	0.017	0.010	0.029	2.5	quasi-
		Kurtosis	3.07	3.28	2.86		
21 November 2018, 16:10:14 - 16:55:31	(11 R _e , 13 R _e)	χ^2	0.010	0.049	0.009	0.9	quasi-⊥
		Kurtosis	3.84	3.75	2.92		
29 November 2018, 22:42:34 - 23:31:01	(11 R _e , 8 R _e)	χ^2	0.008	0.005	0.008	5	quasi-
		Kurtosis	3.04	2.90	3.10		
05 December 2018, 14:53:23 - 15:20:13	(12 R _e , 7 R _e)	χ^2	0.019	0.015	0.013	7.5	quasi-
		Kurtosis	3.39	2.95	2.82		
11 January 2019, 03:22:23 - 03:52:23	(12 R _e , 2 R _e)	χ^2	0.011	0.02	0.028	2.0	quasi-
		Kurtosis	3.52	2.56	2.94		
05 April 2019, 10:58:33 - 11:25:52	(12 R _e , -10 R _e)	χ^2	0.024	0.035	0.086	1.9	quasi-
		Kurtosis	2.66	2.69	2.63		

Quantitative results for the main 40 minute *MMS* interval are shown in the first row entries of Table 3. As figures of merit, the values of the parameter χ^2 are listed along with values of the kurtosis for each component. While the goodness of the Gaussian representation is measured by χ^2 , the closeness of the PDFs to Gaussian distributions can be also be quantified by the kurtosis. The kurtosis for a Gaussian distribution is 3; a kurtosis value greater (less) than 3 represents a super (sub)-Gaussian distribution (Matthaeus et al. 2015). The closeness of the PDFs of the magnetic-field components to Gaussian is clear from Fig. 6 and from the values of χ^2 and kurtoses listed in Table 3. On deriving the power law of the curvature PDF at large values, we also neglect the differences among B_x , B_y , B_z distributions, i.e., the variances of the three components are the same in Eq. 9. For the 40-minute *MMS* interval we have, $\sigma_{B_x} = 7$, $\sigma_{B_y} = 8$, $\sigma_{B_z} = 10$, which can also be seen from the the width of the three distributions shown in Fig. 6.

To draw a more proper conclusion, we further analyze a few other turbulent magnetosheath intervals. Note that for good statistical weight, long intervals are required. Therefore, we select magnetosheath intervals of at least few minutes duration and with no prominent discontinuity. All the selected intervals have large fluctuation amplitude with $B_{\text{rms}}/|\langle \mathbf{B} \rangle| \gtrsim 1$, and the variances of the three components close. Further, we check that each of these intervals exhibits a Kolmogorov “-5/3” spectrum, which is often considered an adequate indicator of well-developed turbulence. The collection of studied magnetosheath intervals are reported in Table 3, where we also report whether each interval is downstream of a quasi-parallel or quasi-perpendicular shock region. The nature of turbulent fluctuations may be

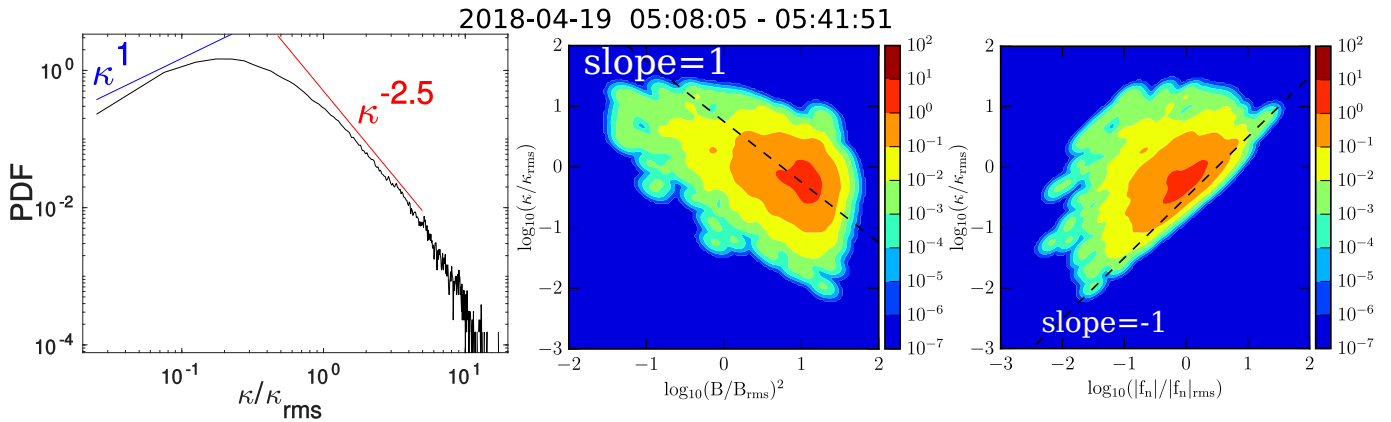


Figure 7. Magnetosheath plasma downstream of a quasi-perpendicular shock observed by MMS on 19 April 2018 (Table 3). Left: PDF of the magnetic field curvature κ normalized to its rms value κ_{rms} . Middle: Joint PDF of curvature κ and the square of magnetic field magnitude B^2 ; Right: Joint PDF of curvature κ and the magnitude of the force $|f_n|$ acting normal to the field lines.

significantly different in the magnetosheath plasma downstream of a quasi-parallel and a quasi-perpendicular shock. The plasma downstream of a quasi-parallel shock is usually found to be more turbulent, relative to that of a quasi-perpendicular shock. The examined intervals include those corresponding to both kinds of shock and with a substantial variation in the normalized fluctuation amplitude $B_{\text{rms}}/|\langle \mathbf{B} \rangle|$.

From Table 3, we see that the Kurtosis lies generally between 2.4 and 4.03, and the values of Kurtosis and the fitness parameter χ^2 do not appear to change systematically from quasi-parallel to quasi-perpendicular shock. Although this is not a fully exhaustive sampling, it appears that turbulent magnetosheath fluctuations are often found in a near-Gaussian state, as is common for fluctuations of the primitive variables in strong homogeneous turbulence (Batchelor 1951; Schumann & Patterson 1978).

C. ADDITIONAL SUPPORTING ANALYSIS

We also perform the analyses presented in the main article, namely Fig. 2 and Fig. 3, for all the intervals listed in Table 3. Again, every interval is found to return reasonably similar result (not shown here), with no systematic variation between quasi-parallel and quasi-perpendicular shocked plasma. The interval studied in the main article corresponds to a quasi-parallel shock. For demonstration, we show the corresponding figures produced for a long magnetosheath interval downstream of a quasi-perpendicular shock, in Fig. 7. Again, the agreement is satisfactory, and the scaling laws appear to hold, in general, for turbulent magnetosheath plasmas.

REFERENCES

- Akhavan-Tafti, M., Slavin, J. A., Sun, W. J., Le, G., & Gershman, D. J. 2019, *Geophysical Research Letters*, 46, 12654, doi: [10.1029/2019GL084843](https://doi.org/10.1029/2019GL084843)
- Batchelor, G. K. 1951, *Proc. Camb. Phil. Soc.*, 47, 359
- Boozer, A. H. 2005, *Rev. Mod. Phys.*, 76, 1071, doi: [10.1103/RevModPhys.76.1071](https://doi.org/10.1103/RevModPhys.76.1071)
- Burch, J. L., Moore, T. E., Torbert, R. B., & Giles, B. L. 2016, *Space Science Reviews*, 199, 5, doi: [10.1007/s11214-015-0164-9](https://doi.org/10.1007/s11214-015-0164-9)
- Dahlin, J. T., Drake, J. F., & Swisdak, M. 2014, *Physics of Plasmas*, 21, 092304, doi: [10.1063/1.4894484](https://doi.org/10.1063/1.4894484)
- Dobrott, D., Nelson, D. B., Greene, J. M., et al. 1977, *Phys. Rev. Lett.*, 39, 943, doi: [10.1103/PhysRevLett.39.943](https://doi.org/10.1103/PhysRevLett.39.943)
- Dunlop, M., Southwood, D., Glassmeier, K.-H., & Neubauer, F. 1988, *Advances in Space Research*, 8, 273, doi: [https://doi.org/10.1016/0273-1177\(88\)90141-X](https://doi.org/10.1016/0273-1177(88)90141-X)
- Fang, Z., Wang, J., Liu, B., & Gong, W. 2012, *Double Pareto Lognormal Distributions in Complex Networks*, ed. M. T. Thai & P. M. Pardalos (Boston, MA: Springer US), 55–80, doi: [10.1007/978-1-4614-0754-6_3](https://doi.org/10.1007/978-1-4614-0754-6_3)
- Franz, M., & Harper, D. 2002, *Planetary and Space Science*, 50, 217, doi: [https://doi.org/10.1016/S0032-0633\(01\)00119-2](https://doi.org/10.1016/S0032-0633(01)00119-2)
- Gershman, D. J., Vinas, A. F., Dorelli, J. C., et al. 2018, *Phys. Plasmas*, 25, 022303, doi: [10.1063/1.5009158](https://doi.org/10.1063/1.5009158)

- Guo, F., Liu, Y.-H., Daughton, W., & Li, H. 2015, *The Astrophysical Journal*, 806, 167, doi: [10.1088/0004-637x/806/2/167](https://doi.org/10.1088/0004-637x/806/2/167)
- Hameiri, E., Laurence, P., & Mond, M. 1991, *Journal of Geophysical Research: Space Physics*, 96, 1513, doi: [10.1029/90JA02100](https://doi.org/10.1029/90JA02100)
- Hoshino, M., Mukai, T., Terasawa, T., & Shinohara, I. 2001, *Journal of Geophysical Research: Space Physics*, 106, 25979, doi: [10.1029/2001JA900052](https://doi.org/10.1029/2001JA900052)
- Jokipii, J. R. 1982, *The Astrophysical Journal*, 255, 716, doi: [10.1086/159870](https://doi.org/10.1086/159870)
- Matthaeus, W. H., Wan, M., Servidio, S., et al. 2015, *Philosophical Transactions of the Royal Society of London A: Mathematical, Physical and Engineering Sciences*, 373, doi: [10.1098/rsta.2014.0154](https://doi.org/10.1098/rsta.2014.0154)
- Mitzenmacher, M. 2004, *Internet Mathematics*, 1, 226, doi: [10.1080/15427951.2004.10129088](https://doi.org/10.1080/15427951.2004.10129088)
- Monin, A. S., & Yaglom, A. M. 1971, *Statistical Fluid Mechanics*, Vol. 1 (Cambridge, Mass.: MIT Press)
- Padhye, N., Smith, C. W., & Matthaeus, W. H. 2001, *Journal of Geophysical Research: Space Physics*, 106, 18 635, doi: [10.1029/2000JA000293](https://doi.org/10.1029/2000JA000293)
- Parashar, T. N., Chasapis, A., Bandyopadhyay, R., et al. 2018, *Phys. Rev. Lett.*, 121, 265101, doi: [10.1103/PhysRevLett.121.265101](https://doi.org/10.1103/PhysRevLett.121.265101)
- Paschmann, G., & Daly, P. W. 1998, *ISSI Scientific Reports Series*, 1. <http://hdl.handle.net/11858/00-001M-0000-0014-D93A-D>
- Pesses, M. E., Eichler, D., & Jokipii, J. R. 1981, *Astrophysical Journal*, Part 2 - Letters to the Editor, 246, L85, doi: [10.1086/183559](https://doi.org/10.1086/183559)
- Petschek, H. E. 1964, in *Physics of Solar Flares*, ed. W. N. Hess, NASA SP-50, Washington, DC, 425–439
- Pollock, C., Moore, T., Jacques, A., et al. 2016, *Space Science Reviews*, 199, 331, doi: [10.1007/s11214-016-0245-4](https://doi.org/10.1007/s11214-016-0245-4)
- Reed, W. J. 2001, *Economics Letters*, 74, 15, doi: [https://doi.org/10.1016/S0165-1765\(01\)00524-9](https://doi.org/https://doi.org/10.1016/S0165-1765(01)00524-9)
- Reed, W. J., & Hughes, B. D. 2002, *Phys. Rev. E*, 66, 067103, doi: [10.1103/PhysRevE.66.067103](https://doi.org/10.1103/PhysRevE.66.067103)
- Reed, W. J., & Jorgensen, M. 2004, *Communications in Statistics - Theory and Methods*, 33, 1733, doi: [10.1081/STA-120037438](https://doi.org/10.1081/STA-120037438)
- Rong, Z. J., Wan, W. X., Shen, C., et al. 2011, *Journal of Geophysical Research: Space Physics*, 116, doi: [10.1029/2011JA016489](https://doi.org/10.1029/2011JA016489)
- Russell, C. T., Anderson, B. J., Baumjohann, W., et al. 2016, *Space Science Reviews*, 199, 189, doi: [10.1007/s11214-014-0057-3](https://doi.org/10.1007/s11214-014-0057-3)
- Schumann, U., & Patterson, G. S. 1978, *Journal of Fluid Mechanics*, 88, 685709, doi: [10.1017/S0022112078002347](https://doi.org/10.1017/S0022112078002347)
- Shen, C., Li, X., Dunlop, M., et al. 2003, *Journal of Geophysical Research: Space Physics*, 108, 1168, doi: [10.1029/2002JA009612](https://doi.org/10.1029/2002JA009612)
- . 2007, *Journal of Geophysical Research: Space Physics*, 112, doi: [10.1029/2005JA011584](https://doi.org/10.1029/2005JA011584)
- Slavin, J. A., Lepping, R. P., Gjerloev, J., et al. 2003, *Journal of Geophysical Research: Space Physics*, 108, SMP 10, doi: [10.1029/2002JA009557](https://doi.org/10.1029/2002JA009557)
- Stawarz, J. E., Eastwood, J. P., Phan, T. D., et al. 2019, *The Astrophysical Journal Letters*, 877, L37, doi: [10.3847/2041-8213/ab21c8](https://doi.org/10.3847/2041-8213/ab21c8)
- Sun, W. J., Slavin, J. A., Tian, A. M., et al. 2019, *Geophysical Research Letters*, 0, doi: [10.1029/2019GL083301](https://doi.org/10.1029/2019GL083301)
- Whang, Y. C. 1977, *Solar Phys.*, 53, 507
- Yang, Y., Wan, M., Matthaeus, W. H., et al. 2019, *Physics of Plasmas*, 26, 072306, doi: [10.1063/1.5099360](https://doi.org/10.1063/1.5099360)